Article

A Theoretical Study of Fe Adsorbed on Pure and Nonmetal (N, F, P, S, Cl)-Doped Ti$_3$C$_2$O$_2$ for Electrocatalytic Nitrogen Reduction

Heng Luo [1,2], Xiaoxu Wang [3], Chubin Wan [1,*], Lu Xie [2], Minhui Song [2] and Ping Qian [1,2]

1 Department of Physics, University of Science and Technology Beijing, Beijing 100083, China; s20190798@xs.ustb.edu.cn (H.L.); qianping@ustb.edu.cn (P.Q.)
2 Beijing Advanced Innovation Center for Materials Genome Engineering, University of Science and Technology Beijing, Beijing 100083, China; b20170555@xs.ustb.edu.cn (L.X.); s20191385@xs.ustb.edu.cn (M.S.)
3 DP Technology, Beijing 100083, China; wangxx@dp.tech
* Correspondence: cbwan@ustb.edu.cn

Abstract: The possibility of using transition metal (TM)/MXene as a catalyst for the nitrogen reduction reaction (NRR) was studied by density functional theory, in which TM is an Fe atom, and MXene is pure Ti$_3$C$_2$O$_2$ or Ti$_3$C$_2$O$_{2-x}$ doped with N/F/P/S/Cl. The adsorption energy and Gibbs free energy were calculated to describe the limiting potentials of N$_2$ activation and reduction, respectively. N$_2$ activation was spontaneous, and the reduction potential-limiting step may be the hydrogenation of N$_2$ to *NNH and the desorption of *NH$_3$ to NH$_3$. The charge transfer of the adsorbed Fe atoms to N$_2$ molecules weakened the interaction of N≡N, which indicates that Fe/MXene is a potential catalytic material for the NRR. In particular, doping with nonmetals F and S reduced the limiting potential of the two potential-limiting steps in the reduction reaction, compared with the undoped pure structure. Thus, Fe/MXenes doped with these nonmetals are the best candidates among these structures.

Keywords: DFT; MXene; nitrogen reduction; electrocatalysis; Gibbs free energy

1. Introduction

Ammonia is a raw material for the production of various fertilizers and is a potential energy source that is easy to store and transport, environmentally friendly, and relatively safe. Ammonia synthesis is important in agricultural production and energy development. However, most ammonia synthesis still relies on the Hubble–Bosch method proposed in the 20th century, which requires harsh reaction conditions (400–600 °C and 20–40 MPa) [1–3]. This method consumes a large amount of energy and causes significant greenhouse gas emissions [4]. In addition, other negative effects, such as adverse effects on the equipment under high-temperature and high-pressure conditions, need to be considered. Therefore, the development of environmentally friendly and less energy-demanding methodologies for NH$_3$ synthesis is urgently needed. Electrocatalytic ammonia synthesis has attracted increasing attention owing to its high efficiency and environmental friendliness. The introduction of electrical energy has a remarkable influence on N$_2$ activation and changes the reaction pathways [5], which is beneficial for the development of new stable and efficient catalysts.

New catalysts can be developed from unique structures, such as core–shell Ni–Au nanoparticles for CO$_2$ hydrogenation [6], or from new materials. The excellent physical, electronic, and chemical properties of two-dimensional (2D) materials have attracted extensive scientific research [7–13]. In addition, 2D materials, such as molybdenum disulfide, graphene, and metal–organic frameworks (MOFs) [14–16], have emerged as potential candidates for electrochemical nitrogen reduction reactions (NRRs). Notably, MXene, a new member of the 2D material family that joined in 2011 [17], has developed rapidly in the past nine years [17–19]. The general formula of MXene is M$_{n+1}$X$_n$T$_x$, where M represents early transition metals (TMs), X represents carbon or nitrogen, T$_x$ represents the surface

functional groups O, OH, or F, and n = 1, 2, 3. MXenes are synthesized by the chemical etching of A layers in the MAX ($M_{n+1}AX_n$) phase. Although a variety of 2D MXenes have been theoretically predicted [20], only a few have been synthesized. MXenes are applied in a wide range of fields, including electrocatalysis [21], hydrogen storage [22,23], lithium-ion batteries [24,25], and supercapacitors [26]. MXene is a potential candidate for electrochemical NRRs (e-NRRs) because of its large specific surface area, adjustable structure, and excellent stability [27–29].

MXene-based electrocatalysts for the e-NRR can be divided into two categories: pure MXene and MXene-based hybrid electrocatalysts [30]. Pure MXene is a potential candidate for the e-NRR. For example, Azofra et al. [31] found that M_3C_2 exhibited good N_2 capture and activation behavior. However, bare-metal atoms on the surface of M_3C_2 are considered active sites [31,32], which tend to bind to functional groups such as oxygen groups; thus, the electrical conductivity is decreased, and the active sites are inactivated. Pure MXene still faces challenges as a catalyst for the e-NRR; therefore, MXene hybrids have been designed. Li et al. [33] loaded nanosized Au particles onto Ti_3C_2 nanosheets (Au/Ti_3C_2) for the e-NRR. Their research indicated that the hybrid is conducive to N_2 chemisorption and decreases the activation energy barrier. Au/Ti_3C_2 shows excellent catalytic performance. MnO_2-decorated $Ti_3C_2T_x$ (MnO_2-$Ti_3C_2T_x$) has also been studied as an efficient electrocatalyst for ammonia synthesis under environmental conditions [34]. MnO_2 and $Ti_3C_2T_x$ synergistically promote electrocatalytic activity to achieve superior catalytic activity. In addition, single-atom catalysts (SACs) have been widely studied because of their low cost, superior performance, and full use of metal atoms. Gao et al. [5] studied the reaction pathways and overpotentials of $Ti_3C_2O_2$-supported TM (Fe, Co, Ru, Rh) SACs. These MXene hybrids, including noble metal–MXene, TM oxide–MXene, and MXene-based SACs, have effectively changed the catalytic performance, providing more possibilities for the screening of new efficient and stable catalysts.

In this study, a 2D MXene, $Ti_3C_2O_2$, was modified with nonmetals (N, F, P, S, and Cl) and adsorbed TM (Fe atom, $Fe/Ti_3C_2O_{2-x}$) to study the catalytic performance of the e-NRR. Gibbs free energy (ΔG) was used to analyze the reaction pathway and limit the potential of each catalyst, and the main potential-limiting steps of the reaction were determined as $*N_2 + H \rightarrow *NHH$ and $*NH_3 \rightarrow NH_3$.

2. Computational Methods

Density functional theory (DFT) calculations were performed using the Vienna ab initio simulation package v. 5.4.4. (University of Vienna, Vienna, Austria) [35,36]. The generalized gradient approximation with Perdew–Burke–Ernzerhof was used as an exchange-correlation function [37]. The projector-augmented wave method was adopted to describe the effect of the core electrons on the valence electron density [38]. The cut-off energy was set to 600 eV. The convergence criteria for the energy and force were 10^{-5} eV and 10^{-2} eV/Å, respectively. The thickness of the vacuum layer was more than 20 Å to avoid interactions in the z-direction, and the x-and y-directions were set as periodic boundary conditions. A $3 \times 3 \times 1$ supercell was used for all the structures. For geometric optimization, the Brillouin zones were sampled with $4 \times 4 \times 1$ Monkhorst–Pack meshes [39], and DFT-D3 was used to accurately describe Van der Waals interactions [40]. Charge transfer was computed by Bader charge population analysis [41,42] and the electron localization function (ELF) was analyzed using the VESTA code [43].

The substitution energies (ΔE_{sub}) of doping different nonmetallic elements (N/F/P/S/Cl) on the surface of $Ti_3C_2O_2$ can be expressed as

$$\Delta E_{sub} = E_{NM-Ti_3C_2O_{2-x}} - E_{Ti_3C_2O_2} + E_O - E_{NM} \tag{1}$$

where E_O and E_{NM} represent the energies of a single O atom and nonmetallic elements (N, F, P, S, Cl), respectively, and were calculated using H_2 [44], H_2O [45], NH_3 [46], HF [47], H_3PO_4 [48], H_2S [49], and HCl [50] from the Open Quantum Materials Database (OQMD) [51,52].

The adsorption energy (ΔE_{ads}) of Fe anchored on NM-Ti$_3$C$_2$O$_{2-x}$ (NM represents the surface nonmetals, O, N, F, P, S, and Cl) was calculated using the following formula:

$$\Delta E_{ads} = E_{Fe/NM-Ti_3C_2O_{2-x}} - E_{NM-Ti_3C_2O_{2-x}} - E_{Fe} \tag{2}$$

ΔG was calculated as described by Nørskov et al. [53]. Under standard reaction conditions, the chemical potential of a proton and electron pair ($\mu[H^+ + e^-]$) is equal to half that of gaseous hydrogen ($\mu[H_2]$). ΔG was calculated using the following formula:

$$\Delta G = \Delta E_{DFT} + \Delta ZPE - T\Delta S - neU + \Delta G_{pH} \tag{3}$$

where ΔE is the potential energy change calculated by DFT, ΔZPE is the zero-point energy correction, and it is calculated by calculating the frequency of the adsorbed species. $T\Delta S$ is the entropy correction, which is usually available from some database, where $T = 298$ K; ΔG_{pH} and neU are the contributions from the pH and electrode potential (U), respectively; n is the number of electrons transferred; U is the applied bias. ΔG_{pH} is defined as

$$\Delta G_{pH} = -k_B T \ln[H^+] = pH \times K_B T \ln 10 \tag{4}$$

where k_B is Boltzmann's constant. For all the calculations, the pH was set to zero. The ΔE_{ads} values of different adsorbates were calculated as follows:

$$\Delta E_{ads} = E_{cat-mol} - E_{cat} - E_{mol} \tag{5}$$

where $\Delta E_{cat-mol}$ is the energy of the entire adsorption structure, E_{cat} is the energy of the catalyst, and E_{mol} is the energy of the adsorbate molecules such as N$_2$ and N$_x$H$_y$.

3. Results and Discussion

3.1. Geometric Structure

Bare Ti$_3$C$_2$ is a hexagonal lattice with P$\bar{3}$m1 group symmetry, five atomic layers of Ti–C–Ti–C–Ti, two exposed Ti layers, and an experimental lattice constant of 3.057 Å [54]. After structural optimization, $a = b = 3.020$ Å, which was in good agreement with the experimental values. Bare MXenes are unstable under relevant NRR operating conditions [55], and they are always functionalized by electronegative functional groups [56], as they are chemically exfoliated from the bulk MAX phase by HF [17,57]. O-terminated Ti$_3$C$_2$ was used for further experiments. There are different possibilities for the adsorption of O on Ti$_3$C$_2$. According to previous studies [5], the most stable structure is O adsorbed at the hollow sites of the contralateral surface Ti atoms, as shown in Figure 1a,b. Nonmetallic elements (N/F/P/S/Cl) were used to modify the Ti$_3$C$_2$O$_2$ surface. ΔE_{sub} indicates the stability of a surface before and after doping with nonmetallic elements. The ΔE_{sub} values for N, F, P, S, and Cl were 1.79, −1.04, 0.81, −0.27, and −1.01 eV, respectively. The structure became more stable after doping with F, S, and Cl when $\Delta E_{sub} < 0$ and became more unstable after doping with N and P when $\Delta E_{sub} > 0$. Among these doping situations, doping with F had the best stability, compared with doping with other nonmetallic elements.

Pure Ti$_3$C$_2$O$_2$ and Ti$_3$C$_2$O$_2$ modified with nonmetallic elements (Figure S1) were used to support single Fe atoms. Two different hollow sites (H1 and H2) and an O-top site on the surface were considered, as shown in Figure 1a. The O-top was unstable, and the E_{ads} values of Fe adsorbed on H1 and H2 are listed in Table 1. Except for the F-doped structures, the Fe atoms preferred to adsorb on the H1 site, as the E_{ads} was smaller. Notably, in the F-doped structure, the Fe atom was adsorbed on the next-nearest H1 site (Figure 1e). As shown in Table 1, the doping of N, F, P, and S facilitates the adsorption of Fe, while it is more difficult for Fe to adsorb on the Cl-doped structure. Figure 1c–h show the most stable adsorption positions for the different catalysts.
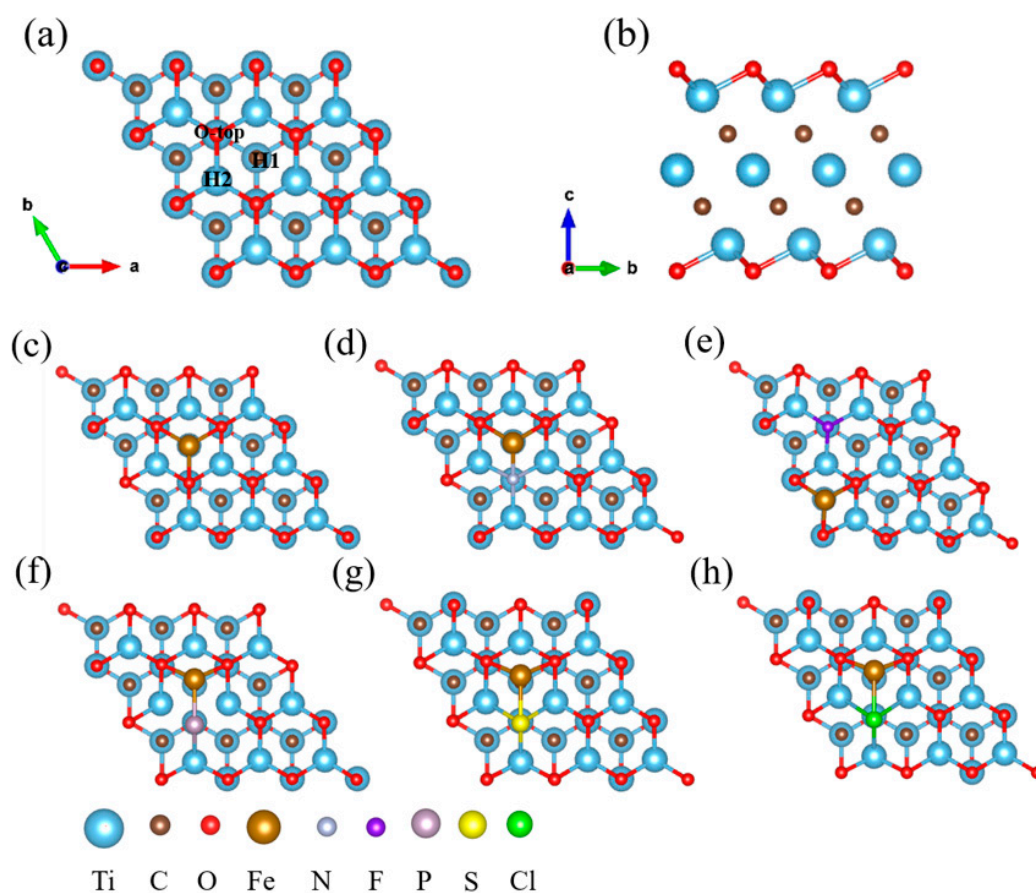
Figure 1. (**a**) Top view and different adsorption sites on $Ti_3C_2O_2$ and (**b**) side view of $Ti_3C_2O_2$. The most stable structure of Fe adsorbed on (**c**) $Ti_3C_2O_2$, (**d**) N-doped $Ti_3C_2O_2$, (**e**) F-doped $Ti_3C_2O_2$, (**f**) P-doped $Ti_3C_2O_2$, (**g**) S-doped $Ti_3C_2O_2$, and (**h**) Cl-doped $Ti_3C_2O_2$.

Table 1. Adsorption energies of Fe adsorbed on different sites and N_2 adsorbed on different catalysts, the charge on N_2, and the charge transferred after N_2 adsorption.

Species	E_{ads} of Fe (eV)		E_{ads} of N_2 (eV)	Charge Transferred on N_2 (e)
	H1	H2		
$Fe/Ti_3C_2O_2$	−3.57	−3.30	−0.92	0.19
Fe/N-$Ti_3C_2O_{2-x}$	−4.32	−3.90	−0.77	0.15
Fe/F-$Ti_3C_2O_{2-x}$	−3.61	−3.60	−0.78	0.18
Fe/P-$Ti_3C_2O_{2-x}$	−5.12	−4.68	−0.55	0.13
Fe/S-$Ti_3C_2O_{2-x}$	−4.33	−4.02	−0.59	0.16
Fe/Cl-$Ti_3C_2O_{2-x}$	−3.39	−3.11	−0.85	0.21

3.2. N_2 Adsorption

Based on the Fe/NM-$Ti_3C_2O_{2-x}$ structure, N_2 adsorption was calculated using E_{ads}. There are two different positions for N_2 adsorption, and advanced research has shown that N_2 adsorption is closer end to end than side to side [5]. Figure 2a–f show the most stable structure of N_2 adsorbed on different catalysts from end to end, and Figure 2g–l show the ELF of these structures. E_{ads} ranged from −0.55 eV to −0.92 eV, which indicates that the N_2 adsorption has strong spontaneity, and the absolute value of E_{ads} from small to large was in the order: Fe/P-$Ti_3C_2O_{2-x}$ < Fe/S-$Ti_3C_2O_{2-x}$ < Fe/N-$Ti_3C_2O_{2-x}$ < Fe/F-$Ti_3C_2O_{2-x}$ < Fe/Cl-$Ti_3C_2O_{2-x}$ < $Fe/Ti_3C_2O_2$ (Table 1). After N_2 adsorption, the N≡N bond lengths in $Fe/Ti_3C_2O_2$, Fe/N-$Ti_3C_2O_{2-x}$, Fe/F-$Ti_3C_2O_{2-x}$, Fe/P-$Ti_3C_2O_{2-x}$, Fe/S-$Ti_3C_2O_{2-x}$, and Fe/Cl-$Ti_3C_2O_{2-x}$ are 1.128, 1.125, 1.129, 1.123, 1.126, and 1.130 Å, respectively. Compared with the N≡N bond length in the gas phase (1.11 Å), all of them became longer. The

calculation of charge transfer is shown in Table 1. The results show that N_2 gains electrons in all these catalysts and the translated charges increase with an increase in the number of valence electrons from N to O or from P to S and Cl in the same period. However, doping with F did not obey this rule, which may be due to the special adsorption site of Fe. Fe was adsorbed on the first nearest H1 site and followed the trend from N to O and F. These findings were consistent with those of Wang et al. [58]. A strong positive correlation exists between the electron gains of N_2 and the change in bond length: N_2 on Fe/Cl-$Ti_3C_2O_{2-x}$ gained the most electrons and had the largest increase in bond length relative to the gas phase, whereas N_2 on Fe/P-$Ti_3C_2O_{2-x}$ gained the least electrons and had the smallest increment in bond length relative to the gas phase.
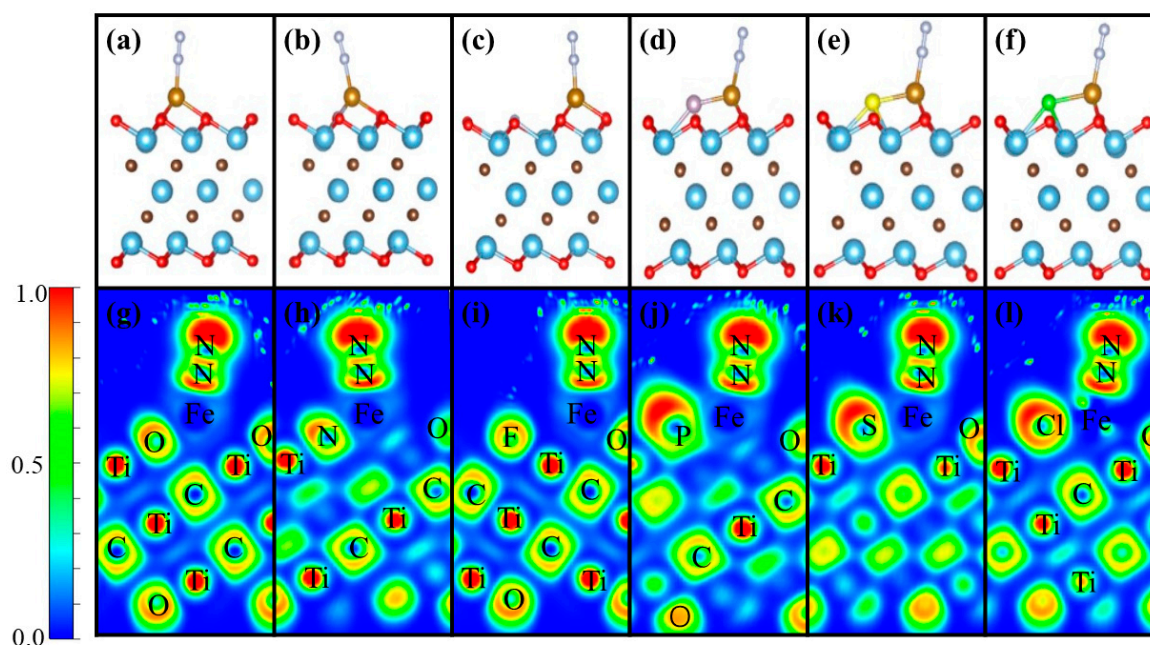

Figure 2. Most stable structures of N_2 adsorbed on (**a**) Fe/$Ti_3C_2O_2$, (**b**) Fe/N-$Ti_3C_2O_{2-x}$, (**c**) Fe/F-$Ti_3C_2O_{2-x}$, (**d**) Fe/P-$Ti_3C_2O_{2-x}$, (**e**) Fe/S-$Ti_3C_2O_{2-x}$, and (**f**) Fe/Cl-$Ti_3C_2O_{2-x}$ and ELFs of N_2 adsorbed on (**g**) Fe/$Ti_3C_2O_2$, (**h**) Fe/N-$Ti_3C_2O_{2-x}$, (**i**) Fe/F-$Ti_3C_2O_{2-x}$, (**j**) Fe/P-$Ti_3C_2O_{2-x}$, (**k**) Fe/S-$Ti_3C_2O_{2-x}$, and (**l**) Fe/Cl-$Ti_3C_2O_{2-x}$.

The partial density of states of N_2 adsorbed on Fe/$Ti_3C_2O_2$ or Fe/NM-$Ti_3C_2O_{2-x}$ (Figure 3) shows spin-up and spin-down of the d orbital of the Fe atom and the p orbital of the N atom. At the Fermi level, almost no spin-up was observed, whereas the spin-down was more obvious, and the d orbital of Fe effectively overlapped with the P orbital of N near the Fermi level. The electrons in the occupied d orbital of Fe/NM-$Ti_3C_2O_{2-x}$ transferred to the antibonding orbitals of N_2, as shown in Table 1, and the adsorbed N_2 on different catalysts gained electrons from 0.13 e to 0.21 e, thus lowering the bond energy of N_2.
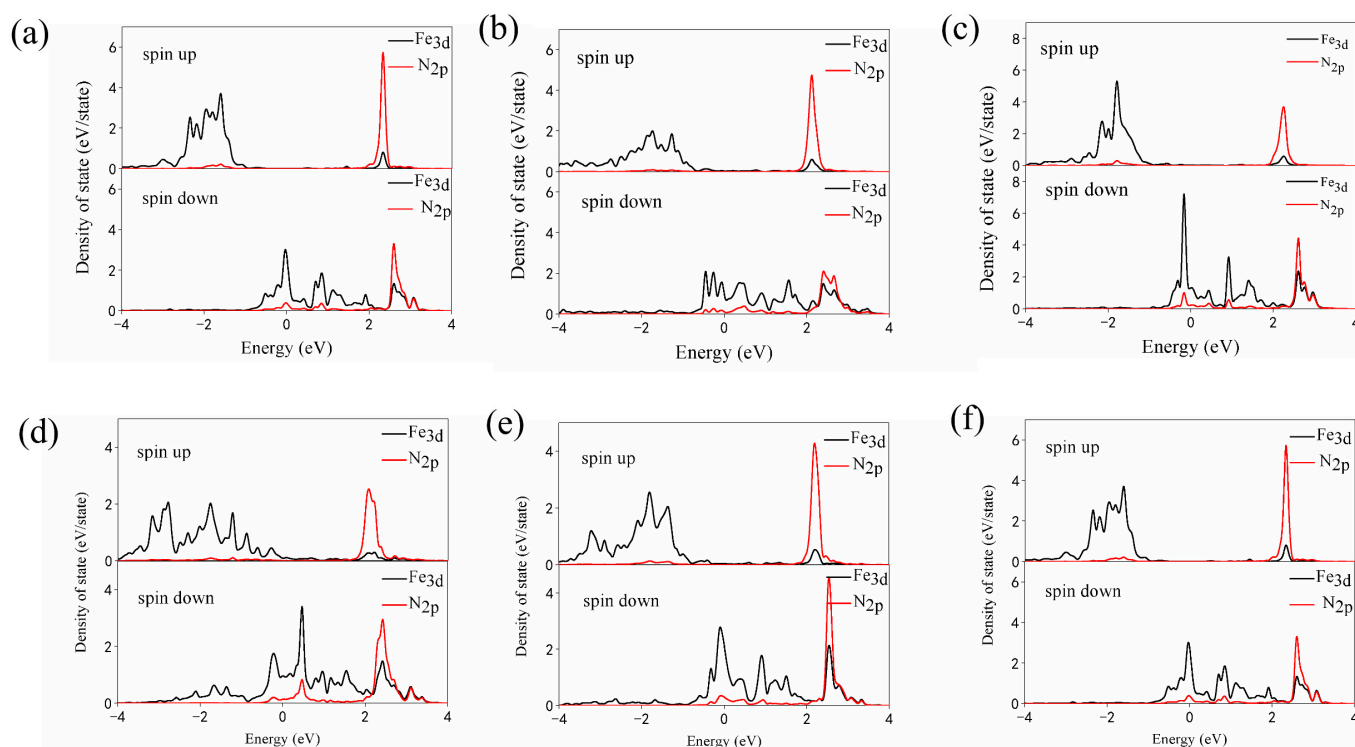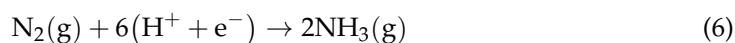
Figure 3. Partial density of states of N_2 adsorbed on (**a**) Fe/Ti$_3$C$_2$O$_2$, (**b**) Fe/N-Ti$_3$C$_2$O$_{2-x}$, (**c**) Fe/F-Ti$_3$C$_2$O$_{2-x}$, (**d**) Fe/P-Ti$_3$C$_2$O$_{2-x}$, (**e**) Fe/S-Ti$_3$C$_2$O$_{2-x}$, and (**f**) Fe/Cl-Ti$_3$C$_2$O$_{2-x}$.

3.3. N_2 Reduction Mechanism

The overall e-NRR reaction on the cathode is

$$N_2(g) + 6(H^+ + e^-) \rightarrow 2NH_3(g) \tag{6}$$

and the anode reactions provide protons and electrons. Liu et al. [59] summarized the mechanism of the e-NRR. The e-NRR is divided into dissociation and association mechanisms by different hydrogenation (protonation and reduction) sequences and the breaking of the N≡N triple bond. In the dissociation mechanism, the N≡N bond is broken during the adsorption process (* denotes the adsorption site).

$$2* + N_2 \rightarrow 2*N \tag{7}$$

Then, two separated N atoms on the surface of the catalysts receive protons and electrons, and ammonia is formed in the last hydrogenation step:

$$*N + H^+ + e^- \rightarrow *NH \tag{8}$$

$$*NH + H^+ + e^- \rightarrow *NH_2 \tag{9}$$

$$*NH_2 + H^+ + e^- \rightarrow *NH_3 \tag{10}$$

$$*NH_3 \rightarrow NH_3 \tag{11}$$

In the association mechanism, the N≡N bond breaks at a certain hydrogenation step. According to the hydrogenation sequence, it can be further classified into distal, alternating, and enzymatic pathways. The hydrogenation step in the enzymatic pathway is similar to that in the alternating pathway; the difference is that N_2 adsorbs side to side in the
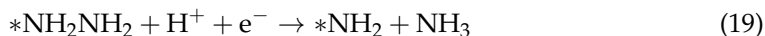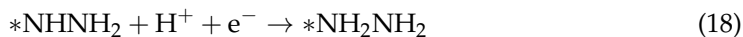
enzymatic pathway, but ends in the distal and alternating pathways. For the distal and alternating pathways, the first two steps are

$$* + N_2 \rightarrow *N_2 \tag{12}$$

$$*N_2 + H^+ + e^- \rightarrow *N_2H \tag{13}$$

In the distal pathway, the N atom moves away from the catalytically gained protons and electrons, releasing the first NH_3 molecule, as follows:

$$*N_2H + H^+ + e^- \rightarrow *NNH_2 \tag{14}$$

$$*NNH_2 + H^+ + e^- \rightarrow *N + NH_3 \tag{15}$$
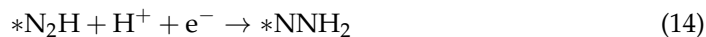
Hydrogenation then occurs on the remaining N atom and releases the second NH_3 molecule according to Reactions (8)–(11). In the alternating pathway, hydrogenation occurs on two newton atoms alternatively, and NH_3 is formed until the $N\equiv N$ bond is completely broken.

$$*N_2H + H^+ + e^- \rightarrow *NHNH \tag{16}$$

$$*NHNH + H^+ + e^- \rightarrow *NHNH_2 \tag{17}$$

$$*NHNH_2 + H^+ + e^- \rightarrow *NH_2NH_2 \tag{18}$$

$$*NH_2NH_2 + H^+ + e^- \rightarrow *NH_2 + NH_3 \tag{19}$$

After the first NH_3 is released, the remaining *NH_2 obtains protons and electrons and releases the second ammonia according to Reactions (10) and (11). Figure 4 shows the other mixed pathways that follow neither the distal nor alternating pathways but a combination of two paths. Optimized structures of all the possible elementary steps in NRR is showed in Figure S2.
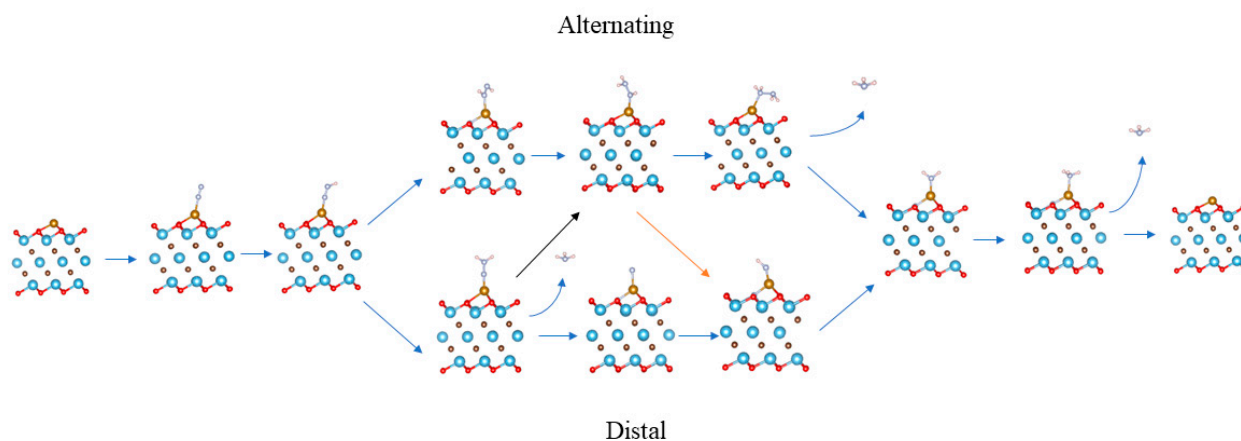

Figure 4. Possible pathway and reaction intermediates for NRR with the associated mechanism. Dark brown, blue, red, brown, light blue, and light pink represent C, Ti, O, Fe, N, and H, respectively.

The ΔG values calculated by DFT calculations considered all correction terms, including the zero-point energy, temperature, and entropy corrections. Table 2 illustrates the E_{ZPE} and entropy corrections (TS) of different reaction intermediates on Fe/$Ti_3C_2O_2$ using the TS values obtained from the National Institute of Standards and Technology [60] at T = 298 K. The catalyst as a substrate is immobilized, although the surface is different, we compared the zero-point energy with the study of Ling [61]; the difference is marginal, as N_2 reduction also occurred on the transition metal atoms in Ling's research, and only the E_{ZPE} of NH_3 was significantly different. NH_3 is a gas phase, not an adsorbent, so other research was also compared [5]. The calculated E_{ZPE} and TS of H_2 are 0.27 and 0.4 eV [60], respectively.

Table 2. E_{ZPE} and TS of different reaction intermediates on Fe/Ti$_3$C$_2$O$_2$, T = 298 K.

Adsorption Species	E_{ZPE} (eV)	E'_{ZPE} (eV)	E_{ZPE} Difference (eV)	TS [60] (eV)
N$_2$	0.15	0.15 [61]	0	0.59
*N≡N	0.19	0.20 [61]	0.01	0.23
*N=NH	0.47	0.49 [61]	0.02	0.20
*N−NH$_2$	0.78	0.82 [61]	0.04	0.25
*N	0.09	0.08 [61]	0.01	0.06
*NH	0.31	0.35 [61]	0.04	0.14
*NH$_2$	0.63	0.65 [61]	0.02	0.18
*NH$_3$	1.00	1.02 [61]	0.02	0.23
*NH=NH	0.81	0.80 [61]	0.01	0.25
*NH−NH$_2$	1.11	1.13 [61]	0.02	0.31
*NH$_2$−NH$_2$	1.50	1.49 [61]	0.01	0.27
NH$_3$	0.92	0.96 [5]	0.04	0.60

As shown in Figure 5a–f, for all structures, the first protonation was likely to generate *NNH species; the ΔG values for Fe/Ti$_3$C$_2$O$_2$, Fe/N-Ti$_3$C$_2$O$_{2-x}$, Fe/F-Ti$_3$C$_2$O$_{2-x}$, Fe/P-Ti$_3$C$_2$O$_{2-x}$, Fe/S-Ti$_3$C$_2$O$_{2-x}$, and Fe/Cl-Ti$_3$C$_2$O$_{2-x}$ increased to 0.90, 1.04, 0.85, 0.99, 0.88, and 1.01 eV, respectively. The second step is more likely to form *NNH$_2$ instead of the *NHNH species in the alternate path, as the energy requirements are higher, and the increments in ΔG for Fe/Ti$_3$C$_2$O$_2$, Fe/N-Ti$_3$C$_2$O$_{2-x}$, Fe/F-Ti$_3$C$_2$O$_{2-x}$, Fe/P-Ti$_3$C$_2$O$_{2-x}$, Fe/S-Ti$_3$C$_2$O$_{2-x}$, and Fe/Cl-Ti$_3$C$_2$O$_{2-x}$ were 0.1, 0.06, 0.12, −0.05, 0.12, and 0.07 eV to form *NNH$_2$, respectively. In the subsequent hydrogenation steps, the intermediate configuration in the alternating pathway was easier to form than the first NH$_3$ molecule desorption in the distal pathway. The first NH$_3$ is not desorbed until the fifth proton is added, and adsorptive *NH$_3$ is formed when the sixth proton is added. The reaction *NNH$_2$ → *NHNH$_2$ → *NH$_2$NH$_2$ → *NH$_2$ → *NH$_3$ is exothermic, and larger energy input is required until the adsorptive *NH$_3$ is desorbed to form the second NH$_3$ molecule. The ΔG values of Fe/Ti$_3$C$_2$O$_2$, Fe/N-Ti$_3$C$_2$O$_{2-x}$, Fe/F-Ti$_3$C$_2$O$_{2-x}$, Fe/P-Ti$_3$C$_2$O$_{2-x}$, Fe/S-Ti$_3$C$_2$O$_{2-x}$, and Fe/Cl-Ti$_3$C$_2$O$_{2-x}$ were 1.95, 1.11, 0.97, 1.07, 1.09, 0.99 eV, respectively. However, it was reported that the use of an acidic electrolyte can promote NH$_3$ desorption, as the protonation of adsorbed NH$_3$ to form NH4$^+$ can easily proceed [62,63], so the actual energy barrier is even smaller. For all these structures, the two potential limiting steps were the first hydrogenation of N$_2$ to form the *NNH species and the last process of NH$_3$ desorption to form the second NH$_3$ molecule. Compared with the original structure, nonmetallic doping was beneficial for the desorption of the last NH$_3$ molecule, but only the doping of F and S was beneficial for the formation of *NNH and NH$_3$.

Figure 6 shows the most possible reaction pathway for different catalysts. All these structures are likely to follow the mixed pathway: N$_2$ → *N$_2$ → *NNH → *NNH$_2$ → *NHNH$_2$ → *NH$_2$NH$_2$ → *NH$_2$ → *NH$_3$ → NH$_3$. In addition, the doping of nonmetals has a remarkable effect on NRR. For N$_2$ adsorption, E_{ads} is reduced, compared with the nondoped structure, which may be the reason why NH$_3$ desorption is easier in the last step. In the hydrogenation process, the doping of different nonmetals also makes each step of the hydrogenation easier or harder. The doping of N, P, and Cl makes it difficult for *N$_2$ to form *NNH, whereas F and S facilitate the formation of *NNH from *N$_2$. From *NNH to *NNH$_2$, only the doping of P shows an obvious impact and makes the transformation occur spontaneously. In comparison, the other doped nonmetals do not show a great effect. The doping of nonmetal also does not have much influence on *NNH$_2$ → *NHNH$_2$ → *NH$_2$NH$_2$ → *NH$_2$ → *NH$_3$, as these reactions are exothermic for all structures. Considering the stability of nonmetal doping, the best catalysts may be Fe/F-Ti$_3$C$_2$O$_{2-x}$ and Fe/S-Ti$_3$C$_2$O$_{2-x}$.
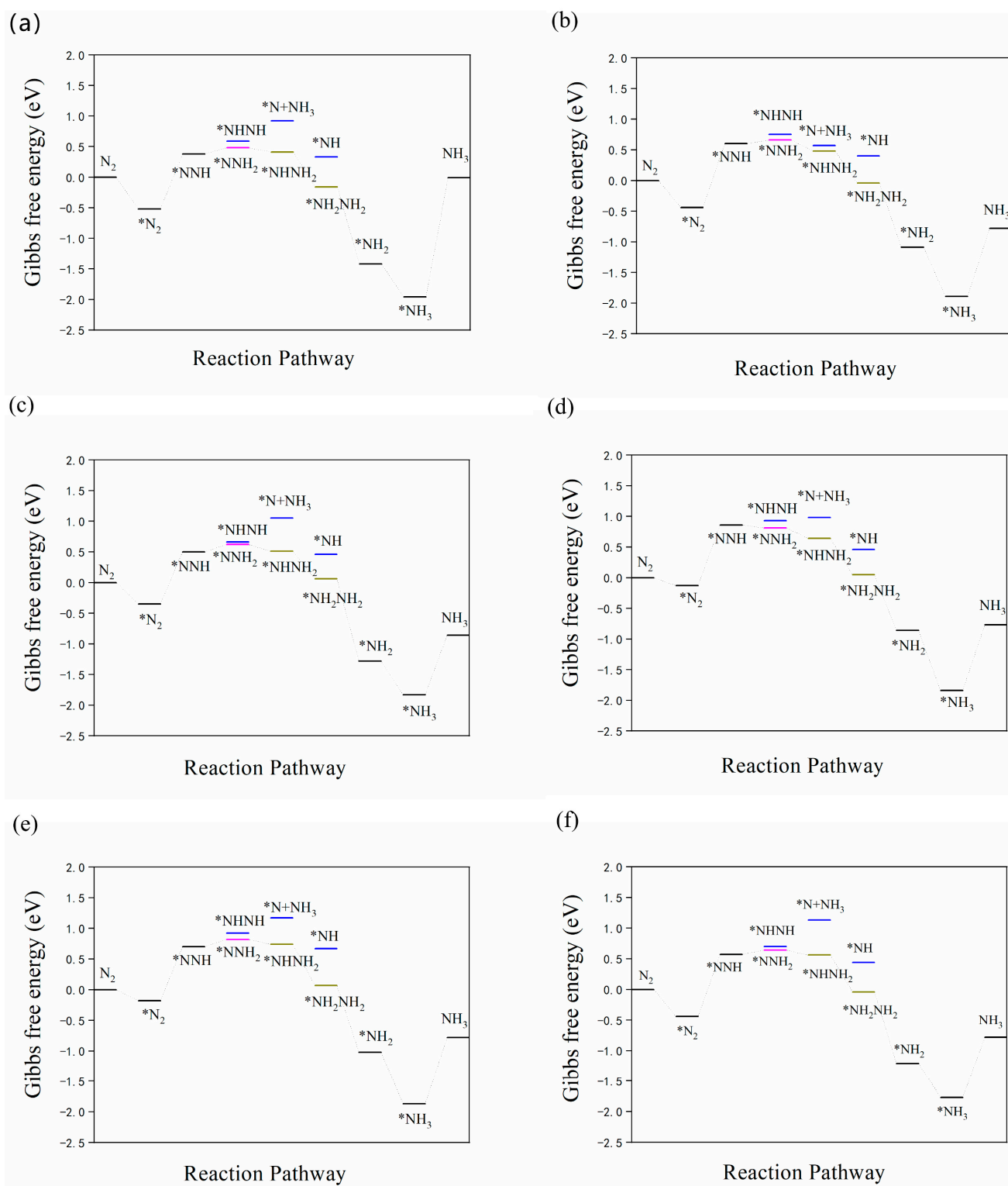
Figure 5. Gibbs free energy diagrams of (**a**) Fe/Ti$_3$C$_2$O$_2$, (**b**) Fe/N-Ti$_3$C$_2$O$_{2-x}$, (**c**) Fe/F-Ti$_3$C$_2$O$_{2-x}$, (**d**) Fe/P-Ti$_3$C$_2$O$_{2-x}$, (**e**) Fe/S-Ti$_3$C$_2$O$_{2-x}$, and (**f**) Fe/Cl-Ti$_3$C$_2$O$_{2-x}$.
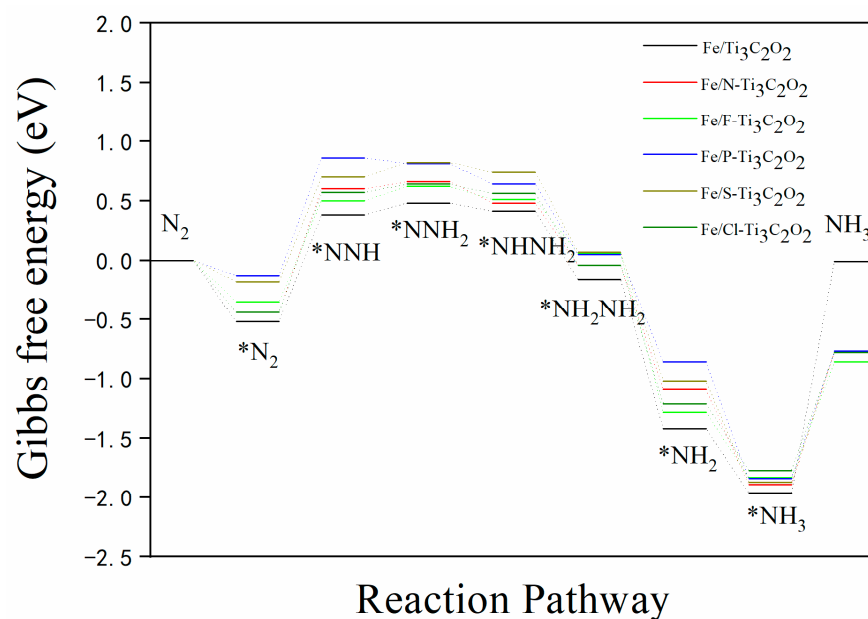
Figure 6. Nitrogen reduction reaction pathways for all structures.

4. Conclusions

The reaction pathway of the TM atom, Fe, adsorbed on pure $Ti_3C_2O_2$ and surface nonmetal (N/F/P/S/Cl)-doped $Ti_3C_2O_2$ as the N_2 reduction reaction catalyst was calculated using DFT. The main limiting steps of the reaction are $*N_2 + H \rightarrow *NNH$ and $*NH_3 \rightarrow NH_3$, and the limiting potentials of the two steps can reach 0.85–1.01 and 0.97–1.95 eV, respectively. Compared with pure $Ti_3C_2O_2$, nonmetal doping has an impact on catalytic performance. The doped nonmetal (N/F/P/S/Cl) reduces the energy barrier to form NH_3 in the last step, and only the doping of F and S is beneficial to the formation of $*NNH$ in the first step and the desorption of $*NH_3$ in the last step. Therefore, the materials doped with F and S are considered better candidate materials for NRR among the tested catalysts. Our research demonstrates a feasible way to search for new NRR catalysts by modifying the surface of MXenes and loading TM atoms as new catalysts.

Author Contributions: The study was planned and designed by H.L., X.W., C.W. and P.Q. DFT calculations were performed by H.L. and X.W. The manuscript was prepared by H.L., L.X. and M.S. H.L., X.W., C.W., L.X., M.S. and P.Q. discussed the results and commented on the manuscript together. All authors have read and agreed to the published version of the manuscript.

Institutional Review Board Statement: Not applicable.

Informed Consent Statement: Not applicable.

Data Availability Statement: The datasets generated during and/or analyzed during the current study are available from the corresponding author.

Conflicts of Interest: The authors declare no conflict of interest.

References

1. Van der Ham, C.J.M.; Koper, M.T.M.; Hetterscheid, D.G.H. Challenges in reduction of dinitrogen by proton and electron transfer. *Chem. Soc. Rev.* **2014**, *43*, 5183–5191. [CrossRef] [PubMed]
2. Guo, C.; Ran, J.; Vasileff, A.; Qiao, S.Z. Rational design of electrocatalysts and photo(electro)catalysts for nitrogen reduction to ammonia (NH_3) under ambient conditions. *Energy Environ. Sci.* **2018**, *11*, 45–56. [CrossRef]
3. Zhao, Y.; Zhao, Y.; Shi, R.; Wang, B.; Waterhouse, G.I.N.; Wu, L.Z.; Tung, C.H.; Zhang, T. Tuning Oxygen Vacancies in Ultrathin TiO_2 Nanosheets to Boost Photocatalytic Nitrogen Fixation up to 700 nm. *Adv. Mater.* **2019**, *31*, 1806482. [CrossRef] [PubMed]
4. Smill, V.; Streatfeild, R.A. Enriching the earth: Fritz Haber, Carl Bosch, and the transformation of world food production. *Electron. Green J.* **2002**, *43*, 622–623. [CrossRef]
5. Gao, Y.; Zhuo, H.; Cao, Y.; Sun, X.; Zhuang, G.; Deng, S.; Zhong, X.; Wei, Z.; Wang, J. A theoretical study of electrocatalytic ammonia synthesis on single metal atom/MXene. *Cuihua Xuebao/Chin. J. Catal.* **2019**, *40*, 152–159. [CrossRef]
6. Wang, R. The dynamics of the peel. *Nat. Catal.* **2020**, *3*, 333–334. [CrossRef]
7. Sun, M.; Liu, H.; Qu, J.; Li, J. Earth-Rich Transition Metal Phosphide for Energy Conversion and Storage. *Adv. Energy Mater.* **2016**, *6*, 1600087. [CrossRef]
8. Cong, L.; Xie, H.; Li, J. Hierarchical Structures Based on Two-Dimensional Nanomaterials for Rechargeable Lithium Batteries. *Adv. Energy Mater.* **2017**, *7*, 1601906. [CrossRef]
9. Fu, Q.; Bao, X. Surface chemistry and catalysis confined under two-dimensional materials. *Chem. Soc. Rev.* **2017**, *46*, 1842–1874. [CrossRef]
10. Novoselov, K.S.; Mishchenko, A.; Carvalho, A.; Neto, A.H.C. 2D materials and van der Waals heterostructures. *Science* **2016**, *353*, aac9439. [CrossRef]
11. Shan, A.; Teng, X.; Zhang, Y.; Zhang, P.; Xu, Y.; Liu, C.; Li, H.; Ye, H.; Wang, R. Interfacial electronic structure modulation of Pt-MoS2 heterostructure for enhancing electrocatalytic hydrogen evolution reaction. *Nano Energy* **2022**, *94*, 106913. [CrossRef]
12. Su, Y.; Cao, S.; Shi, L.; Qian, P. Investigation of biaxial strain behavior and phonon-limited mobility for γ graphyne: First-principles calculation. *J. Appl. Phys.* **2021**, *130*, 195703. [CrossRef]
13. Chan, H.; Wang, H.; Song, K.; Zhong, M.; Shi, L.; Qian, P. Origin of phonon-limited mobility in two-dimensional metal dichalcogenides. *J. Phys. Condens. Mat.* **2022**, *34*, 013003. [CrossRef] [PubMed]
14. Suryanto, B.H.R.; Kang, C.S.M.; Wang, D.; Xiao, C.; Zhou, F.; Azofra, L.M.; Cavallo, L.; Zhang, X.; Macfarlane, D.R. Rational Electrode-Electrolyte Design for Efficient Ammonia Electrosynthesis under Ambient Conditions. *ACS Energy Lett.* **2018**, *3*, 1219–1224. [CrossRef]
15. Deng, J.; Liu, C. Boron-Doped Graphene Catalyzes Dinitrogen Fixation with Electricity. *Chem* **2018**, *4*, 1773–1774. [CrossRef]
16. Luo, S.; Li, X.; Zhang, B.; Luo, Z.; Luo, M. MOF-Derived Co_3O_4@NC with Core-Shell Structures for N_2 Electrochemical Reduction under Ambient Conditions. *ACS Appl. Mater. Interfaces* **2019**, *11*, 26891–26897. [CrossRef]
17. Naguib, M.; Kurtoglu, M.; Presser, V.; Lu, J.; Niu, J.; Heon, M.; Hultman, L.; Gogotsi, Y.; Barsoum, M.W. Two-dimensional nanocrystals produced by exfoliation of Ti_3AlC_2. *Adv. Mater.* **2011**, *23*, 4248–4253. [CrossRef]
18. Zhang, P.; Wang, D.; Zhu, Q.; Sun, N.; Fu, F.; Xu, B. Plate-to-Layer Bi_2MoO_6/MXene-Heterostructured Anode for Lithium-Ion Batteries. *Nano-Micro Lett.* **2019**, *11*, 81. [CrossRef]
19. Liu, Y.T.; Zhang, P.; Sun, N.; Anasori, B.; Zhu, Q.Z.; Liu, H.; Gogotsi, Y.; Xu, B. Self-Assembly of Transition Metal Oxide Nanostructures on MXene Nanosheets for Fast and Stable Lithium Storage. *Adv. Mater.* **2018**, *30*, 1707334. [CrossRef]
20. Tang, Q.; Zhou, Z.; Chen, Z. Innovation and discovery of graphene-like materials via density-functional theory computations. *Wiley Interdiscip. Rev. Comput. Mol. Sci.* **2015**, *5*, 360–379. [CrossRef]
21. Liu, A.; Liang, X.; Ren, X.; Guan, W.; Gao, M.; Yang, Y.; Yang, Q.; Gao, L.; Li, Y.; Ma, T. Recent Progress in MXene-Based Materials: Potential High-Performance Electrocatalysts. *Adv. Funct. Mater.* **2020**, *30*, 2003437. [CrossRef]
22. Hu, Q.; Sun, D.; Wu, Q.; Wang, H.; Wang, L.; Liu, B.; Zhou, A.; He, J. MXene: A new family of promising hydrogen storage medium. *J. Phys. Chem. A* **2013**, *117*, 14253–14260. [CrossRef] [PubMed]
23. Wu, X.; Wang, Z.; Yu, M.; Xiu, L.; Qiu, J. Stabilizing the MXenes by Carbon Nanoplating for Developing Hierarchical Nanohybrids with Efficient Lithium Storage and Hydrogen Evolution Capability. *Adv. Mater.* **2017**, *29*, 1607017. [CrossRef] [PubMed]
24. Naguib, M.; Come, J.; Dyatkin, B.; Presser, V.; Taberna, P.L.; Simon, P.; Barsoum, M.W.; Gogotsi, Y. MXene: A promising transition metal carbide anode for lithium-ion batteries. *Electrochem. Commun.* **2012**, *16*, 61–64. [CrossRef]
25. Luo, J.; Tao, X.; Zhang, J.; Xia, Y.; Huang, H.; Zhang, L.; Gan, Y.; Liang, C.; Zhang, W. Sn^{4+} Ion Decorated Highly Conductive Ti_3C_2 MXene: Promising Lithium-Ion Anodes with Enhanced Volumetric Capacity and Cyclic Performance. *ACS Nano* **2016**, *10*, 2491–2499. [CrossRef]
26. Yan, J.; Ren, C.E.; Maleski, K.; Hatter, C.B.; Anasori, B.; Urbankowski, P.; Sarycheva, A.; Gogotsi, Y. Flexible MXene/Graphene Films for Ultrafast Supercapacitors with Outstanding Volumetric Capacitance. *Adv. Funct. Mater.* **2017**, *27*, 1701264. [CrossRef]
27. Zhong, Y.; Xia, X.H.; Shi, F.; Zhan, J.Y.; Tu, J.P.; Fan, H.J. Transition metal carbides and nitrides in energy storage and conversion. *Adv. Sci.* **2015**, *3*, 1500286. [CrossRef]
28. Li, Z.; Wu, Y. 2D Early Transition Metal Carbides (MXenes) for Catalysis. *Small* **2019**, *15*, 1804736. [CrossRef]
29. Zhao, Q.; Zhu, Q.; Miao, J.; Zhang, P.; Wan, P.; He, L.; Xu, B. Flexible 3D Porous MXene Foam for High-Performance Lithium-Ion Batteries. *Small* **2019**, *15*, 1904293. [CrossRef]

30. Sun, J.; Kong, W.; Jin, Z.; Han, Y.; Ma, L.; Ding, X.; Niu, Y.; Xu, Y. Recent advances of MXene as promising catalysts for electrochemical nitrogen reduction reaction. *Chin. Chem. Lett.* **2020**, *31*, 953–960. [CrossRef]

31. Azofra, L.M.; Li, N.; Macfarlane, D.R.; Sun, C. Promising prospects for 2D d^2-d^4 M_3C_2 transition metal carbides (MXenes) in N_2 capture and conversion into ammonia. *Energy Environ. Sci.* **2016**, *9*, 2545–2549. [CrossRef]

32. Li, N.; Chen, X.; Ong, W.J.; Macfarlane, D.R.; Zhao, X.; Cheetham, A.K.; Sun, C. Understanding of Electrochemical Mechanisms for CO_2 Capture and Conversion into Hydrocarbon Fuels in Transition-Metal Carbides (MXenes). *ACS Nano* **2017**, *11*, 10825–10833. [CrossRef] [PubMed]

33. Liu, D.; Zhang, G.; Ji, Q.; Zhang, Y.; Li, J. Synergistic Electrocatalytic Nitrogen Reduction Enabled by Confinement of Nanosized Au Particles onto a Two-Dimensional Ti_3C_2 Substrate. *ACS Appl. Mater. Interfaces* **2019**, *11*, 25758–25765. [CrossRef]

34. Kong, W.; Gong, F.; Zhou, Q.; Yu, G.; Ji, L.; Sun, X.; Asiri, A.M.; Wang, T.; Luo, Y.; Xu, Y. An MnO_2-Ti_3C_2T: X MXene nanohybrid: An efficient and durable electrocatalyst toward artificial N_2 fixation to NH_3 under ambient conditions. *J. Mater. Chem. A* **2019**, *7*, 18823–18827. [CrossRef]

35. Kresse, G.; Furthmüller, J. Efficiency of ab-initio total energy calculations for metals and semiconductors using a plane-wave basis set. *Comput. Mater. Sci.* **1996**, *6*, 15–50. [CrossRef]

36. Kresse, G.; Furthmüller, J. Efficient iterative schemes for ab initio total-energy calculations using a plane-wave basis set. *Phys. Rev. B Condens. Matter Mater. Phys.* **1996**, *54*, 11169. [CrossRef]

37. Perdew, J.P.; Burke, K.; Ernzerhof, M. Generalized gradient approximation made simple. *Phys. Rev. Lett.* **1996**, *77*, 3865–3868. [CrossRef]

38. Blöchl, P.E. Projector augmented-wave method. *Phys. Rev. B* **1994**, *50*, 17953–17979. [CrossRef]

39. Monkhorst, H.J.; Pack, J.D. Special points for Brillouin-zone integrations. *Phys. Rev. B* **1976**, *13*, 5188–5192. [CrossRef]

40. Grimme, S.; Antony, J.; Ehrlich, S.; Krieg, H. A consistent and accurate ab initio parametrization of density functional dispersion correction (DFT-D) for the 94 elements H-Pu. *J. Chem. Phys.* **2010**, *132*, 154104. [CrossRef]

41. Henkelman, G.; Arnaldsson, A.; Jónsson, H. A fast and robust algorithm for Bader decomposition of charge density. *Comput. Mater. Sci.* **2006**, *36*, 354–360. [CrossRef]

42. Sanville, E.; Kenny, S.D.; Smith, R.; Henkelman, G. Improved grid-based algorithm for Bader charge allocation. *J. Comput. Chem.* **2007**, *28*, 899–908. [CrossRef] [PubMed]

43. Momma, K.; Izumi, F. VESTA 3 for three-dimensional visualization of crystal, volumetric and morphology data. *J. Appl. Crystallogr.* **2011**, *44*, 1272–1276. [CrossRef]

44. Ozerov, R.; Kogan, V.; Zhdanov, G.; Kukhto, O. The crystalline structure of solid isotopes of hydroxy. *Sov. Phys. Cryst.* **1962**, *6*, 507–508.

45. Bernal, J.D.; Fowler, R.H. A theory of water and ionic solution, with particular reference to hydrogen and hydroxyl ions. *J. Chem. Phys.* **1933**, *1*, 515–548. [CrossRef]

46. Olovsson, I.; Templeton, D.H. X-ray study of ammonia and ammonia monohydrate. *Am. Crystallogr. Assoc. Progr. Abstr.* **1959**, *12*, 832–836.

47. Johnson, M.W.; Sándor, E.; Arzi, E. The crystal structure of deuterium fluoride. *Acta Crystallogr. Sect. B Struct. Crystallogr. Cryst. Chem.* **1975**, *31*, 1998–2003. [CrossRef]

48. Furberg, S.; Landmark, P.; Gardell, S.; Magnéli, A.; Magnéli, A.; Pestmalis, H.; Åsbrink, S. The Crystal Structure of Phosphorous Acid. *Acta Chem. Scand.* **1957**, *11*, 1505–1511. [CrossRef]

49. Cockcroft, J.K.; Fitch, A.N. The solid phases of deuterium sulphide by powder neutron diffraction. *Z. Krist. New Cryst. Struct.* **1990**, *193*, 1–19. [CrossRef]

50. Sándor, E.; Farrow, R.F.C. Crystal structure of solid hydrogen chloride and deuterium chloride. *Nature* **1967**, *213*, 171–172. [CrossRef]

51. Saal, J.E.; Kirklin, S.; Aykol, M.; Meredig, B.; Wolverton, C. Materials design and discovery with high-throughput density functional theory: The open quantum materials database (OQMD). *JOM* **2013**, *65*, 1501–1509. [CrossRef]

52. Kirklin, S.; Saal, J.E.; Meredig, B.; Thompson, A.; Doak, J.W.; Aykol, M.; Rühl, S.; Wolverton, C. The Open Quantum Materials Database (OQMD): Assessing the accuracy of DFT formation energies. *NPJ Comput. Mater.* **2015**, *1*, 15010. [CrossRef]

53. Rossmeisl, J.; Logadottir, A.; Nørskov, J.K. Electrolysis of water on (oxidized) metal surfaces. *Chem. Phys.* **2005**, *319*, 178–184. [CrossRef]

54. Mashtalir, O.; Naguib, M.; Mochalin, V.N.; Dall'Agnese, Y.; Heon, M.; Barsoum, M.W.; Gogotsi, Y. Intercalation and delamination of layered carbides and carbonitrides. *Nat. Commun.* **2013**, *4*, 1716. [CrossRef] [PubMed]

55. Johnson, L.R.; Sridhar, S.; Zhang, L.; Fredrickson, K.D.; Raman, A.S.; Jang, J.; Leach, C.; Padmanabhan, A.; Price, C.C.; Frey, N.C.; et al. MXene Materials for the Electrochemical Nitrogen Reduction-Functionalized or Not? *ACS Catal.* **2020**, *10*, 253–264. [CrossRef]

56. Gao, G.; O'Mullane, A.P.; Du, A. 2D MXenes: A New Family of Promising Catalysts for the Hydrogen Evolution Reaction. *ACS Catal.* **2017**, *7*, 494–500. [CrossRef]

57. Tong, Y.; He, M.; Zhou, Y.; Zhong, X.; Fan, L.; Huang, T.; Liao, Q.; Wang, Y. Electromagnetic wave absorption properties in the centimetre-band of $Ti_3C_2T_x$ MXenes with diverse etching time. *J. Mater. Sci. Mater. Electron.* **2018**, *29*, 8078–8088. [CrossRef]

58. Wang, X.; Su, Y.; Song, M.; Song, K.; Chen, M.; Qian, P. Design single nonmetal atom doped 2D Ti_2CO_2 electrocatalyst for hydrogen evolution reaction by coupling electronic descriptor. *Appl. Surf. Sci.* **2021**, *556*, 149778. [CrossRef]

59. Liu, D.; Chen, M.; Du, X.; Ai, H.; Lo, K.H.; Wang, S.; Chen, S.; Xing, G.; Wang, X.; Pan, H. Development of Electrocatalysts for Efficient Nitrogen Reduction Reaction under Ambient Condition. *Adv. Funct. Mater.* **2021**, *31*, 2008983. [CrossRef]
60. National Institute of Standards and Technology. Available online: https://janaf.nist.gov/ (accessed on 30 December 2021).
61. Ling, C.; Ouyang, Y.; Li, Q.; Bai, X.; Mao, X.; Du, A.; Wang, J. A General Two-Step Strategy–Based High-Throughput Screening of Single Atom Catalysts for Nitrogen Fixation. *Small Methods* **2019**, *3*, 1800376. [CrossRef]
62. Chun, H.J.; Apaja, V.; Clayborne, A.; Honkala, K.; Greeley, J. Atomistic Insights into Nitrogen-Cycle Electrochemistry: A Combined DFT and Kinetic Monte Carlo Analysis of NO Electrochemical Reduction on Pt(100). *ACS Catal.* **2017**, *7*, 3869–3882. [CrossRef]
63. Clayborne, A.; Chun, H.-J.; Rankin, R.B.; Greeley, J. Elucidation of Pathways for NO Electroreduction on Pt(111) from First Principles. *Angew. Chem.* **2015**, *127*, 8373–8376. [CrossRef]